Polarization dependence of light transmission through individual nanoapertures in metal films

Kaan T. Gunay, Patrick W. Flanigan, Pei Liu, and Domenico Pacifici*

School of Engineering, Brown University, 184 Hope St., Providence, Rhode Island 02912, USA
**Corresponding author: Domenico_Pacifici@brown.edu*

Received December 5, 2013; revised April 1, 2014; accepted April 1, 2014;
posted April 1, 2014 (Doc. ID 202193); published April 23, 2014

We present a systematic study of light transmission through individual nanoscale apertures (rectangular slits and circular holes) etched in a 300-nm-thick silver film. Transmission spectra were obtained as functions of aperture shape and size, as well as the wavelength and polarization state of the normally incident light beam. By varying the wavelength of the incident light in the 550–750 nm range and the characteristic dimensions of the apertures from ~100 nm to 10 μm, a universal behavior of light transmission is revealed. The role of incident polarization and aperture dimensions is investigated in detail, and a clear transition from the geometric regime of light transmission (large apertures) to the subwavelength regime is demonstrated experimentally. A quantitative analysis of the extinction coefficient is reported for rectangular slits, demonstrating that they can act as efficient linear polarizers with extinction ratios >100:1. Finally, a method to convert far-field to near-field data is developed for circular apertures, revealing the contribution of surface plasmon polaritons to the decrease in light transmission for apertures below the cutoff condition.

OCIS codes: (050.1970) Diffractive optics; (310.6628) Subwavelength structures, nanostructures; (260.3910) Metal optics; (120.7000) Transmission; (240.6680) Surface plasmons.
http://dx.doi.org/10.1364/JOSAB.31.001150

1. INTRODUCTION

Light transmission through apertures in opaque films has been a focus of scientific inquiry for centuries, ever since Grimaldi reported that light propagating in a dense medium is not only subject to the laws of refraction and reflection, but can also be diffracted, in particular by a small aperture [1]. In 1897, Lord Rayleigh theoretically derived the cutoff condition for light propagating through a tiny hole etched in a perfect conductor and showed that light transmission could be significantly attenuated when the hole diameter ($2a$) was smaller than half the wavelength (λ) of the incident light [2]. The ratio of these quantities is a key parameter in determining the behavior of optical transmission. Bethe's landmark 1944 paper demonstrated that the intensity of the transmitted light (T) is proportional to the fourth power of this ratio for a circular aperture in a perfectly conducting film (that is, $T \propto (2a/\lambda)^4$) [3]. This ratio is also important in defining the "regime" of light propagation behavior, and the mathematical methods required to study it. When the ratio is large (that is, the aperture is much larger than the wavelength), the system is in the geometric regime, so called because classical ray-tracing analysis can be used to model light propagation and transmission. When the ratio is small ($2a/\lambda < 0.5$ for circular apertures), the system is in the subwavelength regime, and new analytical methods have to be employed to calculate diffraction and light transmission. In a series of theoretical papers, Bouwkamp derived analytical solutions for the problem of light transmission through an infinitesimally thin film with infinite conductivity, although only valid for hole diameters much smaller than the incident wavelength [4,5]. Several authors have further refined the analytical framework and numerical calculations, adding important contributions to the field of light diffraction by individual circular or rectangular apertures in perfectly conducting screens as well as including the effects of finite conductivity and surface plasmons supported by real metals [6–11].

From an experimental standpoint, it was suggested that individual nanoapertures could be used to build a superresolution optical microscope [12], and the experimental demonstration that nanoholes could show significant transmission paved the way to the exciting possibility of effectively building an optical microscope that could overcome the diffraction limit of conventional optical elements [13].

Several researchers have reported sparse data hinting to the exponential decrease of light transmission through a single hole in a real metal film as a function of decreasing hole diameter [14] or increasing film thickness [15]. It has also been reported that flanking an individual hole with corrugations (such as grooves on each side of a slit, or concentric rings surrounding an individual hole) can lead to intensity modulation (i.e., enhancement or suppression) of light transmission [16–18], as well as beaming of light transmitted through the aperture [19].

In 1998 Ebbesen *et al.* found that the transmitted light intensity could be enhanced at certain wavelengths in the visible to near-infrared spectral range by periodically distributing nanoscale holes in the metal plane, using distances comparable to or smaller than the wavelength of the incident light [20]. Although similar phenomena had previously been demonstrated for radio [21] and far-infrared [22] waves, demonstrating enhanced transmission for light in the visible range with wavelengths on the order of ~500 nm requires a significant experimental effort and state-of-the-art nanofabrication techniques to etch holes with dimensions on the same order

of magnitude over a relatively large area while still maintaining high precision.

The observed effect of enhanced optical transmission was at first explained as the result of the nanohole array acting like a grating coupler, where the incident light is coupled to surface plasmon polaritons (SPPs); transmission would then be enhanced as the SPP modes tunneled through the film [23–25]. An alternative explanation has been proposed, based on optical interference between the incident light beam at each hole location and the SPPs generated by diffractive light scattering at neighboring holes [26–30]. This picture, while simple, shows excellent agreement with the experimental results, and it is able to correctly predict and explain the spectral features (i.e., position of the intensity maxima and minima in the normalized light transmission spectra) as well as the intensity enhancement and suppression factors, not only for periodic, but also for random and quasi-periodic arrays of nanoholes [30]. The role of the quasi-cylindrical wave (also known as a creeping wave), a second component of the total scattered field that is highly localized at the nanocorrugation, has also been the focus of significant research [31,32]. In particular, Ref. [31] shows that the quasi-cylindrical wave has a significant contribution in the observed enhanced optical transmission.

Other studies on enhanced optical transmission have examined the relationship between aperture shape and the presence of localized plasmon resonances [33–36], as well as the roles played by the taper angle of the aperture cross section [37] and the polarization state of the incident light [38].

Most studies on light transmission through subwavelength apertures in metal films infer the transmission properties of individual holes from collective measurements performed on arrays of virtually identical holes [39,40]. However, even for studies employing arrays of identical apertures with large inter-hole spacing, it can be troublesome to decouple periodicity effects from the properties of each individual aperture (e.g., size, shape, and polarization response), thus making it challenging to analyze how a single hole behaves as an isolated scattering center in its interaction with light. Although studies on single apertures have been performed in the terahertz range (see, for example, Ref. [41], among others), demonstrating similar effects using light in the visible range poses significant experimental challenges since the experiments needed to reveal the subwavelength regime of light transmission through such systems require state-of-the-art nanofabrication techniques to realize orders of magnitude smaller apertures (on the scale of ~100 nm as opposed to ~100 μm for terahertz studies).

This report presents a comprehensive experimental investigation of light transmission through individual nanoscale apertures etched in a real metal (silver), as functions of incident wavelength and linear polarization state, and aperture size and shape (either circles or rectangles). Silver was chosen for its high conductivity; although gold is better in terms of avoiding oxidization, gold exhibits strong absorption in part of the wavelength range studied here [42]. Rather than focusing on a narrowly defined data set with a specific aperture size or wavelength, multiple parameters were varied simultaneously to give a more detailed and exhaustive overview. Additionally, the parameters were varied with a small step size (e.g., the characteristic size of the apertures varied from 100 to 2000 nm in steps of 50 nm, while the wavelength was varied from 550 to 750 nm with a spectral resolution of 0.3 nm), which allowed the transmission behavior of the devices to be characterized as they transitioned from the subwavelength to the geometric regime. By using a model introduced by Yi *et al.* [43] for circular aperture transmission, a method for correcting far-field data to near-field data was obtained that shows excellent agreement with 3D finite-difference time-domain (FDTD) simulations. As for the rectangular slits, studying transmission as a function of polarization angle produced a model for predicting the polarization dependence of the system relying only on the parallel and perpendicular states, as well as a quantitative report of the extinction ratio across the same spectral and aperture size ranges.

2. METHODS

A. Experimental

A layer of silver (300 nm thick) was deposited via electron beam evaporation on top of a quartz glass slide that was previously cleaned with an RCA cleaning procedure, opportunely modified and optimized to reduce the formation of unwanted pinholes in the metal film that could affect the transmission measurements. All of the apertures studied in this report were etched on the same slide using focused ion beam (FIB) milling (using Ga^+ ions with an acceleration voltage of 30 kV, and a current of 9 pA). The apertures were divided into three groups (in separate columns on the same slide, as seen in Fig. 1: (1) rectangular slits with a fixed length but variable width; (2) rectangular slits with a fixed width but variable length; and (3) circular holes with a variable diameter. Using an automated script to carefully control the stage position, ion beam focus, and stigmation, three different sets of nanoapertures were etched on the same film, arranged according to a matrix consisting of three columns (aperture type) and 40

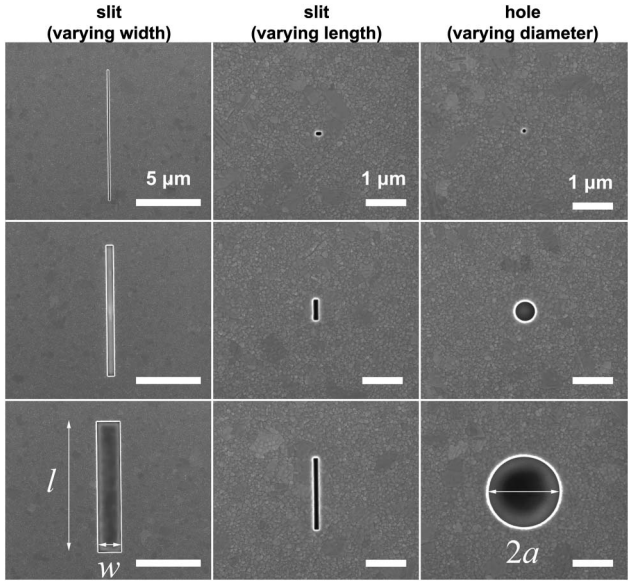

Fig. 1. Sample SEM images of the nanoapertures studied in this paper. The apertures are sorted into three groups, each corresponding to a different column in the figure. The first group contains rectangular apertures of fixed length ($l = 10$ μm) and variable width ($w = 50$, 500, and 1750 nm shown here). The second group contains rectangular apertures of fixed width ($w = 100$ nm) and variable length ($l = 50$, 500, and 1750 nm shown here). The third group contains circular apertures of variable diameter ($2a = 50$, 500, and 1750 nm shown here).

rows (variable aperture size), for a total of 120 different apertures. The three columns were separated by 0.5 mm to ensure that no crosstalk would occur between the various apertures, so that the optical properties of the apertures could be measured independently from each other. Figure 1 shows example scanning electron microscope (SEM) images of these apertures. In group 1, the length was $l = 10$ μm, and the width varied from $w = 50$ nm to 2 μm in steps of 50 nm. In group 2, the width was $w = 100$ nm, and lengths varied from $l = 50$ nm to 2 μm in steps of 50 nm. In group 3, the diameter varied from $2a = 50$ nm to 2 μm, in steps of 50 nm.

Figure 2(a) shows a schematic of the experimental setup. The original light source was a broadband halogen lamp. The randomly polarized beam was sent through a linear polarizer (Thorlabs LPVIS) with high extinction ratio ($>100,000:1$ over a broad wavelength range), and collimated by a 30× microscope condenser with a 1 mm aperture diaphragm before being normally incident upon the silver film. Specular reflection from the sample was used to ensure normal incidence of the light beam onto the sample. The light transmitted through each aperture in the metal film was then collected using a 40× objective lens with a 3-mm-long working distance, and a numerical aperture (NA) of 0.6—corresponding to a collection half-angle (θ_c) of 36.9°—and dispersed using a single-grating spectrograph and projected onto the 100 × 1340 linear array of a CCD camera; the transmitted light intensity spectrum through each nanoaperture was then recorded individually by selecting an appropriate region of interest.

The schematic in Fig. 2(b) provides more information about the system and explains some of the conventions used in this report. The transmission spectra are functions of (1) the incident wavelength (550 nm $< \lambda <$ 750 nm), (2) the angle of polarization, defined with respect to the long axis of the slit ($0 \le \phi_P \le 90°$, in steps of 1°)—when considering oblique incidence in the x–z plane, $\phi_P = 0°$ corresponds to transverse magnetic (TM) while $\phi_P = 90°$ corresponds to transverse electric (TE) illumination conditions, and (3) aperture size (for rectangles, width w and length l; for circles, diameter $2a$). The TE/TM convention depends on the choice of plane of incidence, so other reports may use a different system [44]. Still, the underlying physics is the same [45]. The spectral curves will be written as $T_{w,l}(\lambda, \phi_P)$ (rectangular) or $T_{2a}(\lambda, \phi_P)$ (circular).

B. Spectral Normalization

In order to account and correct for the intrinsic polarization and wavelength response of the optical elements composing the experimental setup (including the cube beam splitter, the grating in the spectrograph, and the various lenses and beam splitters along the optical path), the transmitted light intensity spectrum through the largest aperture was used to normalize the output transmitted light intensity spectrum of every other aperture in the corresponding set, thus obtaining the normalized transmission T. For example, for set 1 (slits with constant length $l = 10$ μm), the light intensity spectrum measured through each slit was normalized by dividing the raw intensity values at each wavelength by the corresponding intensity values obtained by measuring the raw transmission spectrum through the widest slit ($w = 2$ μm), chosen as the reference. Since the dimensions (length and width) of the reference slit are much larger than the longest wavelength used in the experiments (750 nm), the optical response of the reference slit is well within the geometric regime of light transmission. Therefore, the proposed normalization procedure allows us to properly correct for the spectral dependence of the lamp emissivity, the transmissivity of all optical elements, and the detector spectral efficiency. In order to divide out any intrinsic polarization dependence of the experimental setup, each

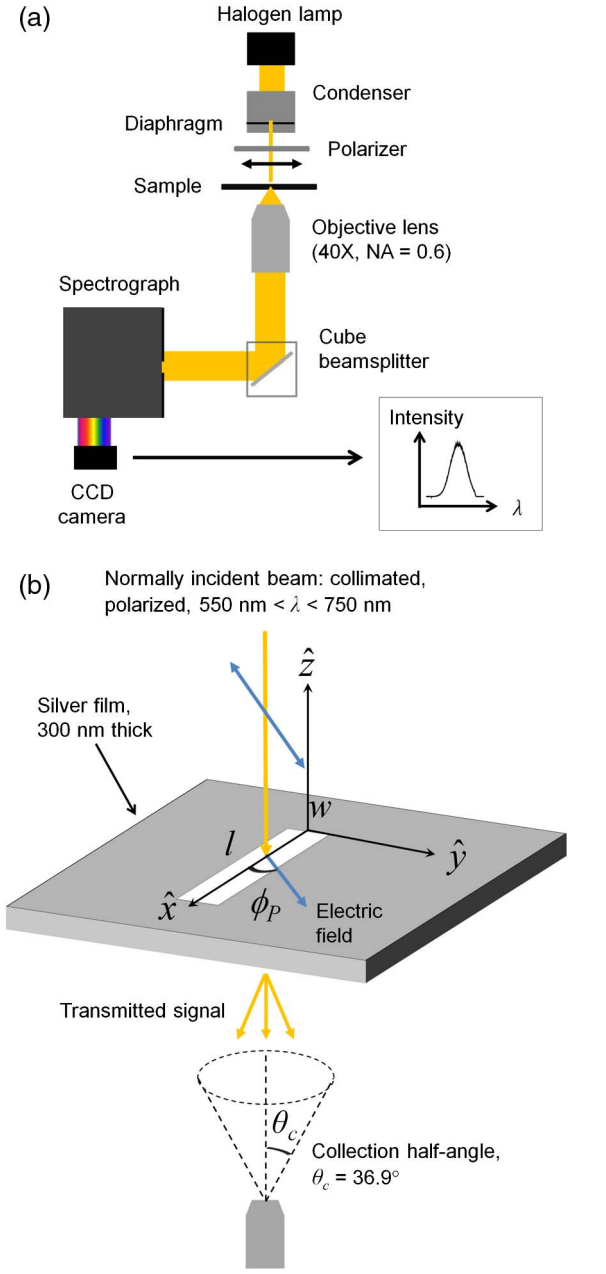

Fig. 2. (a) Schematic of the inverted optical microscope configuration used to collect transmittance data from the nanoscale apertures. The optical path and main optical components are shown. (b) Diagram of the system under study, along with the notation convention used in this paper. For rectangular apertures, the length is given by l (dimension of the long side) and the width is given by w (dimension of the short side). When the aperture is a circle, the characteristic size is given by the diameter ($2a$). The angle of polarization (ϕ_P) is defined as the angle between the long axis of the slit and the incident electric field vector. When considering oblique incidence along the x–z plane, $\phi_P = 0°$ (90°) corresponds to TM (TE) illumination conditions. The collection geometry is also shown.

spectrum was divided by the spectrum through the largest circular hole. This method will be validated experimentally, as reported in Section 3, and will allow us to determine the intrinsic light transmission and polarization properties of each nanoaperture.

C. Simulations

3D FDTD simulations were performed using a commercially available software program (from Lumerical Solutions, Inc.). Using a total field/scattered field technique (with the same spectral range, 550 nm $< \lambda <$ 750 nm) and perfectly matched layers (PMLs) as the boundary conditions on all sides, light was normally incident upon the aperture under investigation (refractive index = 1) in a 300-nm-thick layer of silver (complex refractive index function taken from Palik [46]). Beneath the silver film was a thick layer of SiO_2; all apertures extended 25 nm into the glass layer to simulate effects due to overetching, as experimentally observed during the FIB milling process. Plane monitors were placed in the near field, directly above (for the incident reference fields) and beneath the aperture (to calculate total transmittance).

D. Notation

There are two distinct properties of the transmitted light that will vary depending on whether the system is in the subwavelength or geometric regime. The first property is that the ratio of the spectrally normalized transmittance (T, as obtained via the method reported in Section 2.B) to the cross-sectional area of the aperture (A) will remain constant in the geometric regime (regardless of aperture shape or size), but may be variable in the subwavelength regime (in other words, the T/A curve should be flat in the geometric regime, regardless of all other factors). To facilitate this analysis, much of the data presented below will be plotted in terms of the quantity $\tau = T/A$, i.e., the normalized-to-area light transmission. The expression of τ for circular apertures in full notation is

$$\tau_{2a}(\lambda, \phi_P) = T_{2a}(\lambda, \phi_P)/A_{2a}, \tag{1a}$$

where $A_{2a} = \pi a^2$. The full expression of τ for rectangular apertures is

$$\tau_{w,l}(\lambda, \phi_P) = T_{w,l}(\lambda, \phi_P)/A_{w,l}, \tag{1b}$$

where $A_{w,l} = wl$. The second property is that the transmittance will be independent of the angle of polarization in the geometric regime, but it may be polarization-dependent in the subwavelength regime, especially for nonrotationally symmetric apertures, such as rectangular slits.

3. RESULTS AND DISCUSSION

A. Polarization-Dependent Light Transmission

Figure 3(a) reports the normalized light transmission through a rectangular aperture with $l = 10$ μm and $w = 150$ nm, as a function of both incident wavelength (λ) and polarization angle (ϕ_P, with $0° \le \phi_P \le 90°$ in steps of 1°). The data were normalized against a curve with $l = 10$ μm and $w = 2$ μm, which is guaranteed to be in the geometric regime for the wavelengths used here (550–750 nm)—as mentioned before, this is necessary to factor out any spectral and polarization dependence in the experimental apparatus. The experimental data reported in Fig. 3(a) show significant trends, in particular (1) for any given polarization angle, the normalized transmittance decreases with increasing wavelength and (2) for a given incident wavelength, the normalized transmittance increases as the polarization is varied from 0° to 90°. It may be tempting to reconstruct the experimental curves by just recurring to the two orthogonal polarization states (0° and 90°) considered as an orthonormal basis, according to the following equation:

$$T_{w,l}(\lambda, \phi_p) = T_{w,l}(\lambda, 0°)\cos^2\phi_p + T_{w,l}(\lambda, 90°)\sin^2\phi_p. \tag{2}$$

In other words, once the $T_{w,l}(\lambda, 0°)$ and $T_{w,l}(\lambda, 90°)$ curves have been found for a particular aperture, the transmittance spectrum at any other polarization angle can in principle be reconstructed (due to the symmetry of the system, only the range $0° \le \phi_P \le 90°$ is needed). Figure 3(b) uses Eq. (2) to recreate all of the intermediary curves. The good agreement (within experimental error) between Figs. 3(a) and 3(b) demonstrates the validity of this approach, at least from a qualitative point of view; the origin of the small disagreement between experimental and reconstructed curves is currently under investigation, and it will be reported and clarified in more detail elsewhere. Without loss of generality, the remainder of the paper will only report data relative to the two orthogonal polarization angles, i.e., $\phi_P = 0°$ and $\phi_P = 90°$.

B. Rectangular Slit, Variable Width

Figure 4 presents the data for aperture group 1: rectangular slits with variable widths (w) and a constant length of $l = 10$ μm. In all cases, the horizontal axis is the unitless quantity w/λ, which identifies the transmission regime in question (small w/λ on the left for subwavelength; large w/λ on the right for geometric). Each individual curve corresponds to a specific value of w and spans from $\lambda = 550$ to 750 nm. Panels (a) and (b) ($\phi_P = 90°$ and 0°, respectively) are essentially transmission spectra, but with the modifications mentioned above to more easily analyze the data: (1) plot τ (= transmission/area) instead

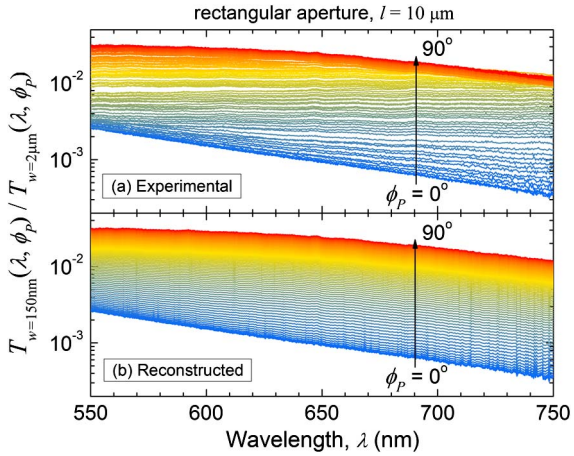

Fig. 3. Using orthogonal polarization states to recreate transmittance spectra at intermediate ϕ_P values ($0° < \phi_P < 90°$). (a) Experimental transmission spectra for a rectangular slit (length $l = 10$ μm, width $w = 150$ nm), normalized against the spectrum of a wider slit ($w = 2$ μm). Each curve corresponds to a different angle of polarization, from 0° to 90° in steps of 1°. (b) Using Eq. (2) and the two experimentally found basis curves ($\phi_P = 0°$ and 90°), the transmission spectrum can be recreated for any intermediate angle.

of just transmission, and (2) normalize against the widest slit (here, $w = 2000$ nm).

As predicted above, the data exhibit a polarization-dependent trend in the subwavelength regime, but not in the geometric regime, and the value of τ stays constant in the geometric regime. To help facilitate the analysis, it will be assumed that the incident beam contains non-normal wavevectors (which is quite reasonable). To fix the ideas, consider an incident wavevector in the plane formed by the surface normal and the long axis of the slit [the x–z plane in Fig. 2(b)]. When in the $\phi_P = 90°$ polarization state, all the electric field components along the direction of incident propagation are zero, corresponding to a TE mode. As such, the observed behavior of the $\phi_P = 90°$ curve can be understood using waveguide analysis. The curve should be flat in the fully idealized scenario, since no cutoff exists for the first TE mode. The propagation wavenumber β for a guided mode propagating through the slit in the z direction is defined as $\beta = \sqrt{(2\pi/\lambda)^2 - (m\pi/l)^2 - (n\pi/w)^2}$, where m and n are non-negative integers $(0, 1, 2, \ldots)$ that cannot equal zero simultaneously. If β is real, the wave will not be "cutoff" as it travels through the slit, corresponding to high transmittance. However, if β is imaginary (which occurs if the argument in the square root function is negative), the amplitude of the wave will decay exponentially as it travels through the slit (i.e., cut off), corresponding to low transmission. The lowest-order TE mode that can be excited is called TE_{10} ($m = 1$, $n = 0$). After some straightforward algebra, the cutoff condition ($\beta = 0$) is revealed to be $l/\lambda = 0.5$. This threshold is never reached for the scenario in Fig. 4(a) (TE mode, $l = 10$ μm; maximum wavelength, $\lambda = 750$ nm), which explains why cutoff is never observed. The small dip in transmittance in the subwavelength regime can be explained by the increased optical diffraction at the output mouth of the slit as w/λ decreases, which causes a decrease in the light intensity collected by the fixed NA objective lens. The collection efficiency (η) of the lens is plotted with the black curve in panel (a), assuming Fraunhofer diffraction behavior (see Appendix A). Since the two data sets (experiments and simulations) in panel (a) exhibit similar trends, it is clear that this provides the explanation as to why the experimental curve deviates from a constant value of 1 for $w/\lambda < 1$.

The data in Fig. 4(b) show a much stronger decrease for $w/\lambda < 0.5$, which cannot be accounted for by the decreased collection efficiency alone. When the angle of polarization is $\phi_P = 0°$, there will be an electric field component along the direction of propagation, but no magnetic field component, thus making it a TM wave. The wavenumber is now $\beta = \sqrt{(2\pi/\lambda)^2 - (m\pi/w)^2 - (n\pi/l)^2}$, with m and n being positive integers $(1, 2, 3, \ldots)$. The cutoff condition is found by considering the lowest-order TM mode (TM_{11}). Considering that $l \gg w$, the cutoff condition ($\beta = 0$) is met when $w/\lambda = 0.5$, or when the slit width is half the incident wavelength. Indeed, there is clearly a strong cutoff at the onset of the subwavelength regime, but the threshold value is closer to $w/\lambda = 0.4$. This can be partially explained by the fact that the wavenumber formula was derived assuming perfectly conducting walls —while silver has a very high conductivity, it is still finite. A red shift in the cutoff condition is therefore expected for rectangular waveguides in real metals, due to the fact that the fields have a finite, yet evanescent, extension into the metal sidewalls, due to the finite conductivity of the metal. Therefore a slit in a real metal, with given width w, can support a mode with slightly longer wavelength than dictated by the cutoff condition for perfect metals [9].

An intermediate light transmission regime is observed in Figs. 4(a) and 4(b), corresponding to values of w and λ such that $0.5 < w/\lambda < 1.5$. This transition between the geometric and the subwavelength regimes is characterized by the wavelength and the aperture dimensions being comparable, so the resonant behavior of the system is more prominent [44]. In this regime, cavity modes can affect the normalized transmittance. For instance, the inset in Fig. 4(a) shows that the wavelength at which maximum normalized transmission occurs, for a given slit width, red shifts with increasing width. The wavelength at which maximum transmission occurs matches the width of the slit (slightly red shifted because of the finite conductivity of the metal), indicating that the maximum in

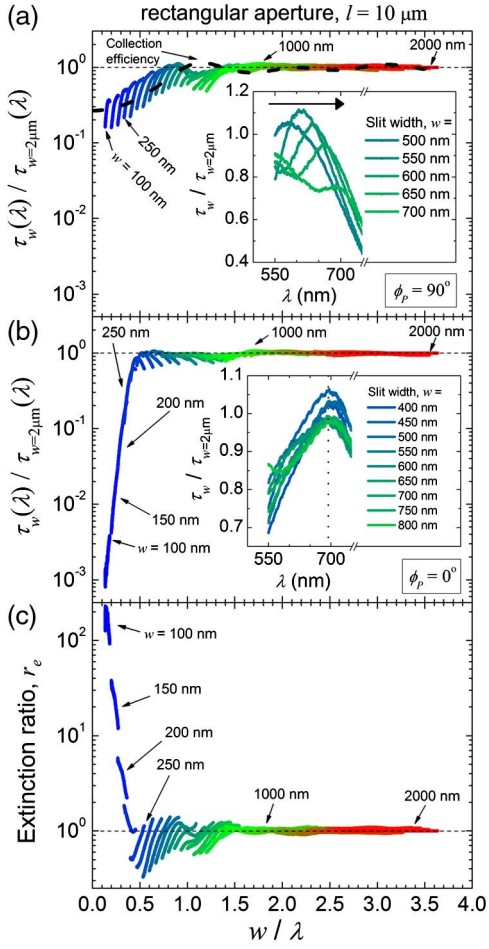

Fig. 4. Relationship between the normalized transmittance-to-area ratio (τ) and the width-to-wavelength ratio for aperture group 1 (rectangular slit, constant length $l = 10$ μm) when (a) $\phi_P = 90°$ (TE) or (b) $\phi_P = 0°$ (TM). In the insets, the vertical axis is the same as the main panels, but now the horizontal axis is wavelength. The dashed black curve in panel (a) is the predicted collection efficiency of the microscope, assuming Fraunhofer diffraction behavior. (c) Experimental extinction ratio, demonstrating the strong polarization dependence in the subwavelength regime. In all three panels, each individual curve corresponds to a specific value of w (ranging from 100 to 2000 nm in steps of 50 nm); each curve is obtained by taking the transmittance spectrum for 550 nm $< \lambda <$ 750 nm, with a spectral resolution of 0.3 nm.

light transmission is determined by a cavity resonant mode across the slit width, when $w = \lambda$ and when the electric field is perpendicular to the long slit axis, i.e., for $\phi_P = 90°$.

On the other hand, the inset in Fig. 4(b) shows that the wavelength at which maximum normalized transmission occurs for the case of an electric field polarized parallel to the long axis of each slit, i.e., $\phi_P = 0°$, is equal to ~690 nm, independently of slit width. This effect can be attributed to the fact that the depth of the silver film in which the slit is etched is ~0.3 μm thick. Assuming a perfect conductor, the minimum wavelength that can fit vertically into this aperture is 0.6 μm. However, when the slits were etched using FIB milling into the 0.3-μm-thick silver film deposited onto a glass substrate, we overetched by ~25–50 nm into the glass substrate to ensure that the slits were indeed etched all the way through and in order to reduce tapering effects. Coupled with the fact that the experiments were conducted on real Ag (instead of a perfect conductor), it is expected that a peak in transmission caused by a resonant cavity mode in the vertical direction (the slit depth) would occur somewhere in the range between 650 and 700 nm, as experimentally observed in the inset of Fig. 4(b).

To quantify the efficiency of rectangular slits as optical polarizers, the extinction ratio (r_e, defined as the ratio of the maximum transmission to the minimum transmission, here taken to be $r_e = T_{w,l}(\lambda, 90°)/T_{w,l}(\lambda, 0°)$) is plotted in Fig. 4(c). Although the trends largely confirm what has already been established—that the system is heavily polarization-dependent in the subwavelength regime, and polarization-independent in the geometric regime—this figure provides an interesting glimpse into how the system transitions from one regime to the other. For an intermediary region (taken here to be $0.5 < w/\lambda < 1.5$), the extinction ratio dips below 1 at some points (that is, transmission for the $\phi_P = 0°$ curve is higher than transmission for the $\phi_P = 90°$ curve) due to the cavity modes responsible for local maxima observed in the insets of Figs. 4(a) and 4(b). Experimentally, the extinction ratio is >100:1, and it is expected to increase for smaller slit widths. In practice, this can be useful for studying plasmonically enhanced photovoltaic devices, where incident light is scattered by a collection of rectangular corrugations for enhanced light trapping—understanding the wavelength and polarization dependence, especially in the visible range, will assist with device optimization [47].

C. Rectangular Slit, Variable Length

Figure 5 presents all of the relevant data for aperture group 2 (variable length, constant width, $w = 100$ nm). Analysis of the underlying physics in this scenario is complicated by the fact that one of the two dimensions of the rectangular slit (i.e., the width) is always subwavelength. In Fig. 5(a), the system is under TE illumination conditions, since $\phi_P = 90°$ (recall that the plane of incidence is hereby defined by the surface normal and the long axis of the slit). In the geometric regime, the normalized transmission-to-area ratio remains practically constant up until $l/\lambda \sim 1$ (since the fundamental TE mode is not cut off in this regime). The curve increases slightly at around $l/\lambda \sim 0.5$ as a result of the formation of a resonant cavity mode. In the subwavelength regime ($l/\lambda < 0.5$), the mode is cut off, resulting in a sharp decrease in transmitted intensity. For TM illumination [$\phi_P = 0°$, Fig. 5(b)], as the slit length is decreased, the transmission steadily increases up until $l/\lambda \sim 0.5$ (while the TM mode is cut off for a very long slit, slits with smaller lengths can support the TE mode, which is no longer cut off, therefore contributing to an increased light transmission); for $l/\lambda < 0.5$ the transmitted intensity starts to decrease again, since both dimensions become subwavelength and the fundamental mode (either TE or TM mode, undistinguishable for $w = l$, by symmetry) becomes cut off. Figure 5(c) reports the extinction ratios r_e for slits with constant $w = 100$ nm and varying length. As shown in the figure, r_e is always >100:1 for long slits, and for any given slit width, the extinction ratio is higher for longer wavelengths, as intuitively expected, since longer wavelengths are characterized by lower transmittance under TM illumination conditions. As l/λ decreases, in particular for $l/\lambda < 0.5$, the extinction ratio drops and it quickly tends to 1, when l and w become equal. This is expected, since when $w = l$, the rectangular slit becomes rotational symmetric with respect to a rotation operation of 90°, and the extinction ratio for such an aperture equals 1.

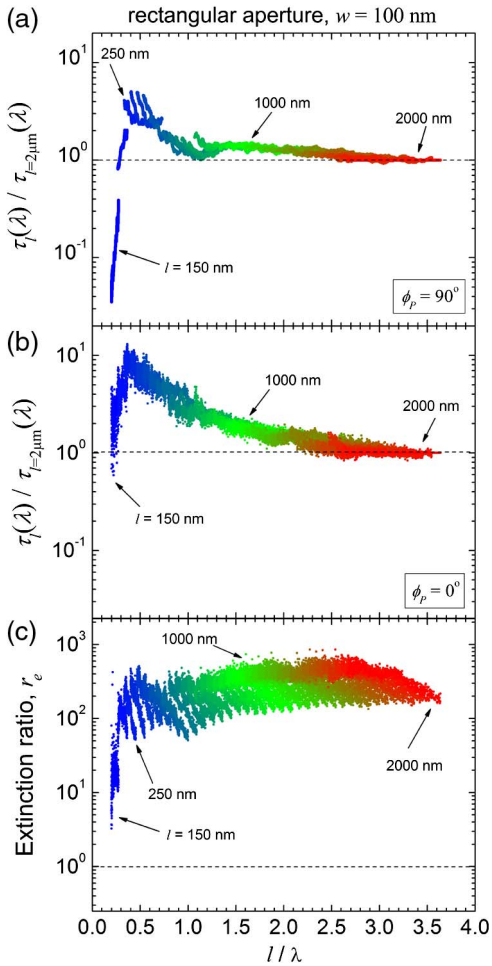

Fig. 5. Relationship between the normalized transmittance-to-area ratio (τ) and the width-to-wavelength ratio for aperture group 2 (rectangular slit, constant width $l = 100$ nm) when (a) $\phi_P = 90°$ (TE) or (b) $\phi_P = 0°$ (TM). (c) Experimental extinction ratio. In all three panels each individual curve corresponds to a specific value of l (ranging from 150 to 2000 nm, in steps of 50 nm); each curve is obtained by taking the transmittance spectrum for 550 nm $< \lambda <$ 750 nm, with a spectral resolution of 0.3 nm.

D. Circular Slit, Variable Diameter

The final data set uses circular apertures, with the diameter ranging from $2a = 250$ to 1950 nm. Both orthogonal polarizations were measured; each curve (for an individual value of $2a$) is the average of the two polarizations (this helps account for any small variability in hole shape). The color curves in Fig. 6(a) are the experimental data for normalized τ; the solid black curve represents the theoretical value of the normalized τ based on the model provided by Yi *et al.* [43]. Reference [43] expanded on the Fraunhofer model of diffraction from circular apertures to create a formula for the scattering cross section, $\sigma(\theta, \varphi)$ (defined as the power flux per solid angle along the direction defined by θ and φ). The full expression is provided in Appendix A, but the basic form is $\sigma(\theta, \phi) = \sigma_0[I_p(\theta)(\cos^2\phi) + I_s(\theta)(\sin^2\phi)]$, where I_p and I_s are the normalized angular distributions of the p and s radiative modes, respectively (these terms depend on the conductivity of the metal, the wavelength, and the radius; σ_0 is independent of angle). To bring the notation in line with this report, the scattering cross section will be written as $\sigma_{2a}(\theta, \varphi, \lambda)$. The angle θ is still between the z axis and the position vector $\mathbf{r}$. The angle φ will be defined via the direction of the electric field vector of the incident beam (that is, $\phi = 0°$ corresponds to the direction of the in-plane component of the incident field). It can easily be shown that

$$\frac{\tau_{2a}(\lambda)}{\tau_{2a=1.95\ \mu\mathrm{m}}(\lambda)} = \frac{\int_{\mathrm{lens}} \sigma_{2a}(\theta, \phi, \lambda)\mathrm{d}\Omega}{\int_{\mathrm{lens}} \sigma_{2a=1.95\ \mu\mathrm{m}}(\theta, \phi, \lambda)\mathrm{d}\Omega} = \frac{\int_0^{\theta_c} \sigma_{2a}(\theta, \lambda)(\sin\theta)\mathrm{d}\theta}{\int_0^{\theta_c} \sigma_{2a=1.95\ \mu\mathrm{m}}(\theta, \lambda)(\sin\theta)\mathrm{d}\theta}, \quad (3)$$

where $d\Omega$ is the solid angle subtended by the objective lens (by symmetry, the azimuthal integration becomes trivial). The agreement between the experimental data and the model helps reaffirm its validity, but the real usefulness of this analysis is shown in Fig. 6(b). Here, the experimental data have been "corrected" by normalizing against the collection efficiency calculated using the diffraction model developed by Yi *et al.* [43] at each point; the gray curve is obtained directly from 3D FDTD simulations. The agreement between the two data sets demonstrates the validity of using this technique to correct for far-field data collection in circular apertures. Note that the model for $\sigma(\theta, \varphi)$ explicitly assumes that the aperture is subwavelength, which allows the analysis to be simplified by only considering the fundamental waveguide mode. The good agreement in the geometric regime ($2a/\lambda > 0.5$) invites further study into how much higher-order waveguide modes affect the output relative to the fundamental mode.

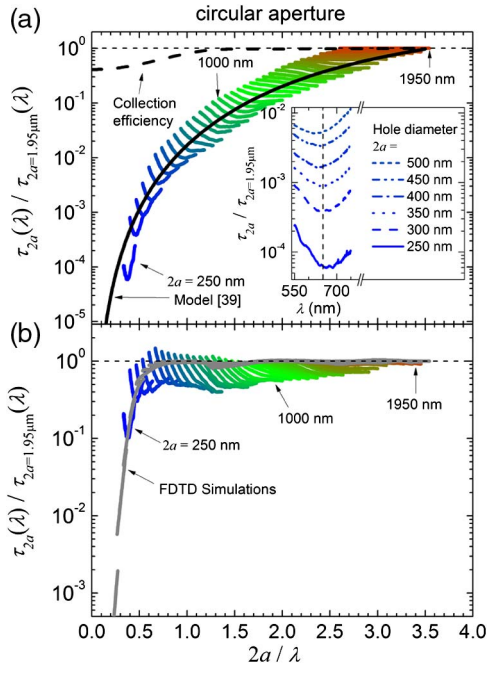

Fig. 6. (a) Relationship between the normalized transmittance-to-area ratio (τ) and the diameter-to-wavelength ratio for the circular apertures (color), along with a theoretical curve based on the work of Yi *et al.* (solid black) [43]. The transmission spectra for both orthogonal polarization states were recorded; the individual curves represent the average value. In the inset, the vertical axis is the same as the main panel, but now the horizontal axis is wavelength. (b) Using the Yi *et al.* model to correct the experimental data. The experimental (color) curves in this panel were obtained by dividing the color curves from panel (a) by the model curve. Gray: simulated normalized τ curves obtained using 3D FDTD simulations. In both panels, each individual curve corresponds to a specific value of $2a$ (ranging from 250 to 1950 nm in steps of 50 nm); each curve is obtained by taking the transmittance spectrum for 550 nm $< \lambda <$ 750 nm, with a spectral resolution of 0.3 nm.

One striking difference between the rectangular slits (Fig. 4, inset) and the circular holes (Fig. 6, inset) is that the individual single-size curves in the former exhibit local maxima as a function of wavelength; in the latter, minima are observed. A possible explanation can be found by recurring to the phase shift light undergoes after it is coupled into a guided SPP mode. More specifically, for propagating SPPs, if the corrugation is rectangular, the phase shift is π [48]; if the corrugation is circular, the phase shift is $\pi/2$ [30]. However, this point certainly deserves further studies.

It is interesting to note that the location of the local extreme is found to be independent of shape. In the ideal case, resonance would occur at $\lambda = 600$ nm, which is twice the nominal thickness of the silver film. For the circular hole data [inset of Fig. 6(a)], the minima occur at around $\lambda = 650$ nm. The discrepancy can be explained by overetching into the glass substrate—circular holes typically require a smaller ion beam dose than rectangular slits to be milled, which explains why this value is slightly smaller than the result in the inset of Fig. 4(b).

Despite being corrected for collection efficiency, the normalized light transmission reported in Fig. 6(b) decreases with decreasing hole diameter, especially for $2a/\lambda < 0.5$. The FDTD data, extracted by using the total light transmitted through a plane monitor placed in the near field of the output mouth of each hole and extending for several micrometers around the hole, also support this trend. A possible explanation for the <1 value of normalized light transmission for $2a/\lambda < 0.5$ is that part of the scattered fields at the output mouth of the aperture is not coupled to radiative modes, but confined at the metal/dielectric interface in the form of SPPs which do not contribute to the measured light transmission. Indeed, subwavelength holes can efficiently couple incident light into propagating SPPs that, while propagating away from the hole, can carry a significant fraction of the incident energy away from the transmitted beam [30], thus justifying the reduced light transmission observed in Fig. 6(b).

4. CONCLUSION

The data presented in this report provide an exhaustive experimental study of light transmission through nanoscale apertures of various size and shape in a real metal film (silver). By varying the size and shape of the nanoapertures as well as the incident wavelength, we have determined a universal behavior of light transmission as a function of the nondimensional quantity represented by the ratio between a characteristic feature dimension of the aperture (such as the width or the length for a rectangular slit, and the diameter for a circular hole) and the free-space wavelength. We have investigated the role of polarization of the incident light on the transmission properties for rectangular nanoslits, quantified their characteristic extinction ratio, and revealed a universal behavior depending only on the dimensionless ratio of slit width divided by wavelength. We have also explained the observed behavior recurring to simple theoretical arguments, and specifically for the case of circular holes, we have demonstrated excellent agreement with a recently developed theory of light diffraction. The experimental data reported in this work can serve as a valuable guide for the development of more accurate theories of light transmission through apertures in real metals.

APPENDIX A

The collection efficiency (η) of a lens is a measure of how effectively it will collect the entire transmitted signal as a function of slit size, wavelength, etc. It is defined as

$$\eta(w,\lambda,\theta_c)=\left(\int_0^{\theta_c}|U(w,\lambda,\theta)|^2\mathrm{d}\theta\right)\Big/\left(\int_0^{\pi/2}|U(w,\lambda,\theta)|^2\mathrm{d}\theta\right), \tag{A1}$$

where $U(w,\lambda,\theta)$ is the complex amplitude of the diffracted wave within the far field and θ_c is the half-angle representing the lens aperture, defined as $\theta_c=\arcsin[\mathrm{NA}/n]$, where NA is the NA of the objective lens and n is the refractive index of air (in this experiment, NA $=0.6$, $n=1$, and $\theta_c=36.9°$). The corresponding maximum collection angle in glass is given by $\theta_{c,\mathrm{glass}}=\arcsin[\mathrm{NA}/n_{\mathrm{glass}}]\approx 24.4°$, such that $\theta_{c,\mathrm{glass}}<\theta_{\mathrm{crit}}$, where θ_{crit} is the critical angle at which total internal reflection between the glass/air interface occurs ($\theta_{\mathrm{crit}}\approx 43.6°$). Therefore the correction to the collection efficiency expression due to reflection losses at the glass/air interface is negligible (not shown). The numerator in Eq. (A1) represents the optical intensity collected by the finite NA lens; the denominator represents a normalization factor (note: due to the azimuthal symmetry of the system, only integration over θ needs to be considered). The Fraunhofer model provides formulas for U in both the rectangular (R) and circular (C) cases. The expressions are

$$U_R(w,\lambda,\theta)=\frac{\sin[u_R(w,\lambda,\theta)]}{u_R(w,\lambda,\theta)}, \tag{A2a}$$

where $u_R(w,\lambda,\theta)=\pi w\ \sin(\theta)/\lambda$, and

$$U_C(a,\lambda,\theta)=2\pi\frac{J_1[u_C(a,\lambda,\theta)]}{u_C(a,\lambda,\theta)}, \tag{A2b}$$

where $u_C(w,\lambda,\theta)=2\pi a\ \sin(\theta)/\lambda$ and $J_1(x)$ is the first Bessel function of the first kind. Figure 4(a) shows a plot of the collection efficiency for rectangular slits as a function of w/λ (gray curve) in the Fraunhofer approximation; Fig. 6(a) shows a plot of the collection efficiency for circular holes as a function of $2a/\lambda$ (gray curve) using the Fraunhofer approximation (dashed line). The solid line has been calculated recurring to Yi's model as described in detail in the main text.

From Ref. [43], the normalized angular distributions from p and s polarizations of the radiative modes are given by

$$I_p(\theta)=\frac{|1+z_s|^2\cos^2(\theta)}{|\cos(\theta)+z_s|^2}\frac{4J_1^2(\Phi)}{\Phi^2}, \tag{A3a}$$

$$I_s(\theta)=\frac{|1+z_s|^2\cos^2(\theta)}{|1+z_s\ \cos(\theta)|^2}\frac{4J_1^2(\Phi)}{(1-\Phi^2/u^2)^2}, \tag{A3b}$$

with $\Phi=ka\ \sin(\theta)$, $k=2\pi/\lambda$, and $u\approx 1.84$ being the first root of the derivative of the Bessel function of the first kind, $J_1'(u)$ (different from what is stated in Ref. [43]). The metal properties are characterized by the surface impedance $z_s=\varepsilon_m^{-1/2}$, where ε_m is the dielectric constant of the metal. The normalization factor σ_0 is a factor that controls the total transmittance but does not affect the radiation pattern. It is equal to $\sigma_0=k^2r^2[4\pi(u^2-1)]^{-1}|E'_{11}|^2|1+z_s|^{-2}$, where E'_{11} is the amplitude of the TE_{11} mode at the hole opening. E'_{11} is a function of wavelength λ, the diameter of the hole $2a$, the metal thickness, and the dielectric constant of the substrate. It should be noted that $I(\theta=0,\phi)=I_p(0)=I_s(0)=1$.

To obtain the normalized transmitted intensity, we calculated the diffraction pattern of the incident light beam from each hole as a function of hole diameter, and numerically evaluated the fraction of the diffracted light intensity collected by the objective lens with fixed NA $=0.6$. More specifically, $\sigma(\theta,\phi)$ was integrated over the variables θ and ϕ, with θ varying from 0 to the collection angle $\theta_c=\arcsin[\mathrm{NA}/n]$ with $n=1$, while ϕ varied from 0 to 2π.

ACKNOWLEDGMENTS

KTG's work was partially funded by a Brown University Undergraduate Teaching and Research Award (UTRA), and by a Maurice R. Seguin Research Stipend. The authors thank R. Zia for helpful discussions. Support from NSF grants DMR-1203186 and CBET-1159255 is also gratefully acknowledged.

REFERENCES

1. F. M. Grimaldi, *Physico Mathesis de Lumine, Coloribus, et Iride, Aliisque Annexis Libri Duo* (Vittorio Bonati, 1665).
2. J. W. Strutt (Lord Rayleigh), "On the passage of electric waves through tubes," J. Phil. Mag. **43**(261), 125–132 (1897).
3. H. A. Bethe, "Theory of diffraction by small holes," Phys. Rev. **66**, 163–182 (1944).
4. C. J. Bouwkamp, "On the diffraction of electromagnetic waves by small circular disks and holes," Philips Res. Rep. **5**, 401–422 (1950).
5. C. J. Bouwkamp, "Diffraction theory," Rep. Prog. Phys. **17**, 35–100 (1954).
6. A. Roberts, "Electromagnetic theory of diffraction by a circular aperture in a thick, perfectly conducting screen," J. Opt. Soc. Am. **4**, 1970–1983 (1987).
7. R. Wannemacher, "Plasmon-supported transmission of light through nanometric holes in metallic thin films," Opt. Commun. **195**, 107–118 (2001).
8. F. J. Garcia de Abajo, "Light transmission through a single cylindrical hole in a metallic film," Opt. Express **10**, 1475–1484 (2002).

9. R. Gordon and A. G. Brolo, "Increased cut-off wavelength for a subwavelength hole in a real metal," Opt. Express **13**, 1933–1938 (2005).
10. F. J. García-Vidal, E. Moreno, J. A. Porto, and L. Martín-Moreno, "Transmission of light through a single rectangular hole," Phys. Rev. Lett. **95**, 103901 (2005).
11. F. J. García-Vidal, L. Martín-Moreno, E. Moreno, L. K. S. Kumar, and R. Gordon, "Transmission of light through a single rectangular hole in a real metal," Phys. Rev. B **74**, 153411 (2006).
12. E. A. Ash and G. Nicholls, "Super-resolution aperture scanning microscope," Nature **237**, 510–512 (1972).
13. A. Lewis, M. Isaacson, A. Harootunian, and A. Murray, "Development of a 500 Å spatial resolution light microscope: I. Light is efficiently transmitted through λ/16 diameter apertures," Ultramicroscopy **13**, 227–231 (1984).
14. D. S. Kim, S. C. Hohng, V. Malyarchuk, Y. C. Yoon, Y. H. Ahn, K. J. Yee, J. W. Park, J. Kim, Q. H. Park, and C. Lienau, "Microscopic origin of surface-plasmon radiation in plasmonic band-gap nanostructures," Phys. Rev. Lett. **91**, 143901 (2003).
15. A. Degiron, H. Lezec, N. Yamamoto, and T. W. Ebbesen, "Optical transmission properties of a single subwavelength aperture in a real metal," Opt. Commun. **239**, 61–66 (2004).
16. T. Thio, K. M. Pellerin, R. A. Linke, H. J. Lezec, and T. W. Ebbesen, "Enhanced light transmission through a single subwavelength aperture," Opt. Lett. **26**, 1972–1974 (2001).
17. F. J. García-Vidal, H. J. Lezec, T. W. Ebbesen, and L. Martín-Moreno, "Multiple paths to enhance optical transmission through a single subwavelength slit," Phys. Rev. Lett. **90**, 213901 (2003).
18. L. Martín-Moreno, F. J. García-Vidal, H. J. Lezec, A. Degiron, and T. W. Ebbesen, "Theory of highly directional emission from a single subwavelength aperture surrounded by surface corrugations," Phys. Rev. Lett. **90**, 167401 (2003).
19. H. J. Lezec, A. Degiron, E. Devaux, R. A. Linke, L. Martin-Moreno, F. J. Garcia-Vidal, and T. W. Ebbesen, "Beaming light from a subwavelength aperture," Science **297**, 820–822 (2002).
20. T. W. Ebbesen, H. J. Lezec, H. F. Ghaemi, T. Thio, and P. A. Wolff, "Extraordinary optical transmission through subwavelength hole arrays," Nature **391**, 667–669 (1998).
21. B. A. Munk, *Frequency Selective Surfaces: Theory and Design* (Wiley, 2000).
22. P. G. Huggard, M. Meyringer, A. Schilz, K. Goller, and W. Prettl, "Far-infrared bandpass filters from perforated metal screens," Appl. Opt. **33**, 39–41 (1994).
23. L. Martín-Moreno, F. J. García-Vidal, H. J. Lezec, K. M. Pellerin, T. Thio, J. B. Pendry, and T. W. Ebbesen, "Theory of extraordinary optical transmission through subwavelength hole arrays," Phys. Rev. Lett. **86**, 1114–1117 (2001).
24. E. Popov, M. Neviere, S. Enoch, and R. Reinisch, "Theory of light transmission through subwavelength periodic hole arrays," Phys. Rev. B **62**, 16100 (2000).
25. W. L. Barnes, W. A. Murray, J. Dintinger, E. Devaux, and T. W. Ebbesen, "Surface plasmon polaritons and their role in the enhanced transmission of light through periodic arrays of subwavelength holes in a metal film," Phys. Rev. Lett. **92**, 107401 (2004).
26. C. Soennichsen, A. C. Duch, G. Steininger, M. Koch, G. von Plessen, and J. Feldmann, "Launching surface plasmons into nanoholes in metal films," Appl. Phys. Lett. **76**, 140–142 (2000).
27. H. J. Lezec and T. Thio, "Diffracted evanescent wave model for enhanced and suppressed optical transmission through subwavelength hole arrays," Opt. Express **12**, 3629–3651 (2004).
28. S.-H. Chang, S. Gray, and G. Schatz, "Surface plasmon generation and light transmission by isolated nanoholes and arrays of nanoholes in thin metal films," Opt. Express **13**, 3150–3165 (2005).
29. H. Gao, J. Henzie, and T. W. Odom, "Direct evidence for surface plasmon-mediated enhanced light transmission through metallic nanohole arrays," Nano Lett. **6**, 2104–2108 (2006).
30. D. Pacifici, H. J. Lezec, L. A. Sweatlock, R. J. Walters, and H. A. Atwater, "Universal optical transmission features in periodic and quasiperiodic hole arrays," Opt. Express **16**, 9222–9238 (2008).
31. F. van Beijnum, C. Retif, C. B. Smiet, H. Liu, P. Lalanne, and M. P. van Exter, "Quasi-cylindrical wave contribution in experiments on extraordinary optical transmission," Nature **492**, 411–414 (2012).
32. P. Lalanne and J. P. Hugonin, "Interaction between optical nano-objects at metallo-dielectric interfaces," Nat. Phys. **2**, 551–556 (2006).
33. K. J. Klein-Koerkamp, S. Enoch, F. B. Segerink, N. F. van Hulst, and L. Kuipers, "Strong influence of hole shape on extraordinary transmission through periodic arrays of subwavelength holes," Phys. Rev. Lett. **92**, 183901 (2004).
34. A. Degiron and T. W. Ebbesen, "The role of localized surface plasmon modes in the enhanced transmission of periodic subwavelength apertures," J. Opt. **7**, S90–S96 (2005).
35. K. L. van der Molen, K. J. Klein-Koerkamp, S. Enoch, F. B. Segerink, N. F. van Hulst, and L. Kuipers, "Role of shape and localized resonances in extraordinary transmission through periodic arrays of subwavelength holes: experiment and theory," Phys. Rev. B **72**, 045421 (2005).
36. F. Przybilla, A. Degiron, C. Genet, T. W. Ebbesen, F. de Leon-Perez, J. Bravo-Abad, F. J. García-Vidal, and L. Martín-Moreno, "Efficiency and finite size effects in enhanced transmission through subwavelength apertures," Opt. Express **16**, 9571–9579 (2008).
37. T. Søndergaard, S. I. Bozhevolnyi, J. Beermann, S. M. Novikov, E. Devaux, and T. W. Ebbesen, "Extraordinary optical transmission with tapered slits: effect of higher diffraction and slit resonance orders," J. Opt. Soc. Am. B **29**, 130–137 (2012).
38. R. Gordon, A. G. Brolo, A. McKinnon, A. Rajora, B. Leathem, and K. Kavanagh, "Strong polarization in the optical transmission through elliptical nanohole arrays," Phys. Rev. Lett. **92**, 037401 (2004).
39. F. J. García de Abajo, "Colloquium: light scattering by particle and hole arrays," Rev. Mod. Phys. **79**, 1267 (2007).
40. C. Genet and T. W. Ebbesen, "Light in tiny holes," Nature **445**, 39–46 (2007).
41. J. W. Lee, T. H. Park, P. Nordlander, and D. M. Mittleman, "Terahertz transmission properties of an individual slit in a thin metallic plate," Opt. Express **17**, 12660–12667 (2009).
42. P. B. Johnson and R. W. Christy, "Optical constants of the noble metals," Phys. Rev. B **6**, 4370–4379 (1972).
43. J.-M. Yi, A. Cuche, F. de León-Pérez, A. Degiron, E. Laux, E. Devaux, C. Genet, J. Alegret, L. Martín-Moreno, and T. W. Ebbesen, "Diffraction regimes of single holes," Phys. Rev. Lett. **109**, 023901 (2012).
44. F. J. Garcia-Vidal, L. Martin-Moreno, T. W. Ebbesen, and L. Kuipers, "Light passing through subwavelength apertures," Rev. Mod. Phys. **82**, 729–787 (2010).
45. D. M. Pozar, *Microwave Engineering* (Wiley, 1990).
46. E. D. Palik, ed., *Handbook of Optical Constants of Solids* (Academic, 1998).
47. R. A. Pala, J. White, E. Barnard, J. Liu, and M. L. Brongersma, "Design of plasmonic thin-film solar cells with broadband absorption enhancements," Adv. Mater. **21**, 3504–3509 (2009).
48. D. Pacifici, H. J. Lezec, H. A. Atwater, and J. Weiner, "Quantitative determination of optical transmission through subwavelength slit arrays in Ag films: role of surface wave interference and local coupling between adjacent slits," Phys. Rev. B **77**, 115411 (2008).